Tilted spirals and low-temperature skyrmions in Cu_2OSeO_3

M. Crisanti,[1] A. O. Leonov,[2,3,4] R. Cubitt,[5] A. Labh,[1] H. Wilhelm,[6,7] Marcus P. Schmidt,[8] and C. Pappas[1]
[1]*Faculty of Applied Sciences, Delft University of Technology, Mekelweg 15, 2629 JB Delft, The Netherlands*
[2]*Department of Chemistry, Faculty of Science, Hiroshima University, Kagamiyama, Higashi Hiroshima, Hiroshima 739-8526, Japan*
[3]*IFW Dresden, Postfach 270016, D-01171 Dresden, Germany*
[4]*International Institute for Sustainability with Knotted Chiral Meta Matter, Kagamiyama, Higashi Hiroshima, Hiroshima 739-8526, Japan*
[5]*Institut Laue-Langevin, 71 Avenue des Martyrs, CS 20156, 38042 Grenoble, France*
[6]*Diamond Light Source Ltd., OX11 0DE Didcot, United Kingdom*
[7]*Helmholtz-Institute Ulm, Helmholtz-Straße 11, 89081 Ulm, Germany*
[8]*Max Planck Institute for Chemical Physics of Solids, 01187 Dresden, Germany*

(Received 5 December 2022; revised 24 April 2023; accepted 12 May 2023; published 18 July 2023)

The bulk helimagnet Cu_2OSeO_3 represents a unique example in the family of B20 cubic helimagnets exhibiting a tilted spiral and skyrmion phase at low temperatures when the magnetic field is applied along the easy $\langle 001 \rangle$ crystallographic direction. Here we present a systematic study of the stability and ordering of these low-temperature magnetic states. We focus our attention on the temperature and field dependencies of the tilted spiral state that we observe persisting up to above $T = 35$ K, i.e., up to higher temperatures than reported so far. We discuss these results in the frame of the phenomenological theory introduced by Dzyaloshinskii in an attempt to reach a quantitative description of the experimental findings. We find that the anisotropy constants, which are the drivers behind the observed behavior, exhibit a pronounced temperature dependence. This explains the differences in the behavior observed at high temperatures (above $T = 18$ K), where the cubic anisotropy is weak, and at low temperatures (below $T = 18$ K), where a strong cubic anisotropy induces an abrupt appearance of the tilted spirals out of the conical state and enhances the stability of skyrmions.

DOI: 10.1103/PhysRevResearch.5.033033

I. INTRODUCTION

Chiral cubic magnets are at the focus of scientific interest as they are the first systems where chiral magnetic skyrmions have been reported [1–4]. These bulk helimagnets host a set of competing interactions: in decreasing order of magnitude, the magnetic exchange interaction, the Dzyaloshinskii-Moriya interaction (DMI), and smaller terms of the magnetic anisotropy. The fine interplay between these energies determines the characteristics of the magnetic field (H) and temperature (T) phase diagrams of these materials, all showing similar features. Below the ordering temperature T_C the magnetic ground state involves a long-range modulation of the magnetization. For zero applied magnetic field this ground state consists in a multidomain of spirals with a pitch L_D determined by the ratio between the exchange and DMI energies. In addition to these interactions, for cubic helimagnets, the exchange and cubic anisotropies are responsible for pinning the propagation vector of the spirals along specific directions [1,4,5]. With increasing field, however, the modulation direction of all spirals aligns along the direction of the applied field [6–9]. In this set of materials, skyrmions arranged in hexagonal lattices are spontaneously stabilized by thermal fluctuations [1,10] in a small region of the H-T phase diagram, just below T_C, commonly referred to as the skyrmion pocket.

Given the reduced size of the skyrmion pocket, a great deal of effort has been directed towards the engineering of its size and position to enable future skyrmionic applications. In this context, the application of uniaxial strain [11,12], hydrostatic pressure [13,14], electric fields [15–18], and chemical doping [19,20] are all viable ways to modify the skyrmion pocket extension and position.

However, several theoretical models predict the stabilization of skyrmions in bulk cubic helimagnets over a wide range of temperatures below T_C [21–25], and not only in a small region of the phase diagram. In particular, low-temperature skyrmions (LTS) have been recently observed in Cu_2OSeO_3, accompanied by tilted spirals (TS) [26–29], when the magnetic field is applied along the easy $\langle 100 \rangle$ crystallographic direction. That particular behavior can be traced back to the quantum-mechanical character of the magnetic building blocks of Cu_2OSeO_3. These are tetrahedra formed by four Cu^{2+} with $S = \frac{1}{2}$ [30] leading to a particularly strong interplay between the effective single-ion and exchange anisotropies [26]. Through this mechanism, skyrmions, which are more resilient to anisotropy-induced deformations, due to their two-dimensional nature, gain stability [27,29]. The tilted spiral state results from the interplay between cubic and exchange anisotropies and spans a wide range of temperatures, for

---

magnetic fields between H_{C1} and H_{C2}, which mark the transition between the helical and conical states, and the conical and uniformly magnetized, field-polarized, states, respectively.

In the following we present a systematic study of the stability and ordering of the low-temperature magnetic states in bulk Cu_2OSeO_3 that complements previous theoretical and experimental findings [26–29] as we focus on the temperature and field dependencies of the TS state. We find that the reduction of the tilting angle with increasing temperature persists up to much higher temperatures than reported so far, and it is seen as a broadening of the conical scattering. Furthermore, our results show that the transition from the conical to the tilted spiral state changes with temperature, from second order above 18 K to first order at lower temperatures.

We discuss these results in the frame of the phenomenological theory introduced by Dzyaloshinskii [31], which captures the main features of our experimental findings. As compared with previous work, we go a step further towards a quantitative comparison between model and experiment. This leads to the conclusion that the anisotropy constants, which are the drivers behind the observed behavior, exhibit a pronounced temperature dependence explaining the difference between the high-temperature (low cubic anisotropy) and low-temperature (high cubic anisotropy) behavior, separated at the temperature of 18 K, which corresponds to a critical point of our model. Our approach provides a strategy for an in-depth and quantitative understanding of chiral magnets in view of tailoring their properties for future applications.

II. EXPERIMENTAL DETAILS

The small-angle neutron scattering measurements were performed at the D33 instrument of the Institut Laue Langevin (ILL), using a wavelength of $\lambda = 0.8$ nm, with a resolution $\Delta\lambda/\lambda$ of 10%. The sample to detector distance was 12.8 m and the sample was the same single crystal of Cu_2OSeO_3 used in our previous work [26,29]. The sample was glued on an Al support with the $[1\bar{1}0]$ main crystallographic direction vertical. It was placed inside an Oxford Instruments 7-T horizontal-field cryomagnet, which was demagnetized at the beginning of the measurements so that the remanent field was less than 0.1 mT. The cryomagnet was equipped with sapphire windows, each with an opening of $\pm\, 7^\circ$, 90° apart from each other, which allowed for applying the magnetic field $\mu_0\mathbf{H}$ either perpendicular or parallel to the incident neutron beam wave vector $\mathbf{k}_i$.

Our SANS measurements were performed in the configuration schematically shown in Fig. 1(a), with $\mu_0\mathbf{H} \parallel [001]$ and $\mu_0\mathbf{H} \perp \mathbf{k}_i$. As discussed below, this configuration allows for following the evolution of the helical, conical, and tilted spiral Bragg peaks as well as of the skyrmionic scattering when varying the temperature and the magnetic field. In order to determine the scattered intensities associated with these different phases we performed rocking scans by rotating both sample and field around the vertical $[1\bar{1}0]$ axis in steps of 1°, so that $\mu_0\mathbf{H}$ was always parallel to [001]. Due to the limited opening of the cryomagnet windows these scans covered the angular range of $\pm\, 7^\circ$. At each temperature and magnetic field the SANS patterns were obtained by summing the intensities of all rocking scans. For the background correction we used data collected under similar conditions at 10 K and under an applied magnetic field of 2 T.

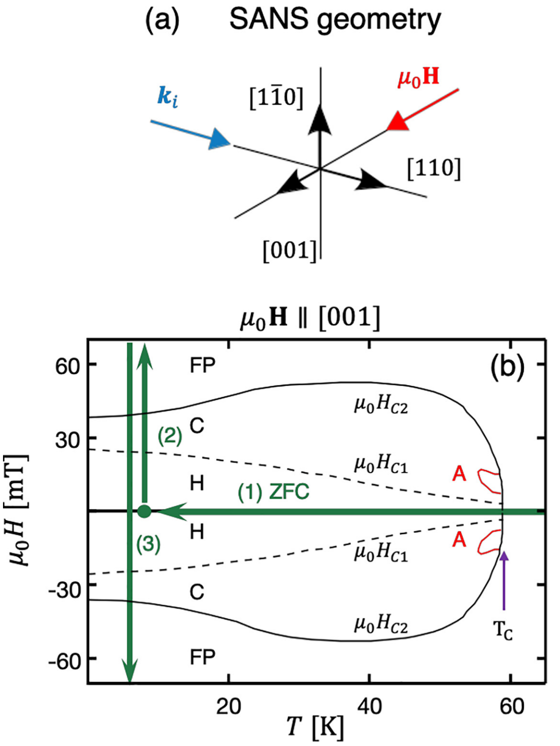

FIG. 1. (a) Schematic representation of the experimental setup, with the $[1\bar{1}0]$ crystallographic axis vertical and perpendicular to the incoming neutron beam propagation vector $\mathbf{k}_i \parallel [110]$, and to the magnetic field $\mu_0\mathbf{H}$, which was applied along [001]. (b) Phase diagram of Cu_2OSeO_3 for $\mathbf{H} \parallel [001]$ (after [26,29]) and schematic representation, by the green arrows, of the experimental procedure used for the SANS measurements. In step 1 the sample was brought to each temperature of interest after zero-field cooling (ZFC) through T_C. Consequently, the magnetic field was increased up to 74 mT, crossing the critical field lines μ_0H_{C1}, from the helical (H) to the conical (C) phase, and μ_0H_{C2} from the conical to the field-polarized (FP) state (step 2). The measurements were then performed by stepwise decreasing the magnetic field to -74 mT (step 3). The figure also depicts in red the boundaries of the A phase, i.e., the pocket near T_C where the skyrmion lattice phase is stabilized.

The measurements were performed using the procedure illustrated by the green arrows in Fig. 1(b). In this figure are also shown the transition lines from the helical to the conical phase μ_0H_{C1}, from the conical to the field-polarized phase μ_0H_{C2}, as well as the A phase, corresponding to the skyrmion lattice pocket. We used the zero-field-cooled, or ZFC, procedure, by bringing the sample to each selected target temperature after cooling it through $T_C \sim 59$ K under zero magnetic field (i.e., under the residual magnetic field of the cryomagnet). Consequently, the magnetic field was increased to 74 mT at 2 K, i.e., well above μ_0H_{C2}. The measurements were then performed by stepwise decreasing the magnetic field down to -74 mT. The starting and ending values of the magnetic field scans were adjusted to be well above μ_0H_{C2} at each target temperature. The magnetic fields have been corrected for demagnetization effects assuming a demagnetization factor of $\frac{1}{3}$.

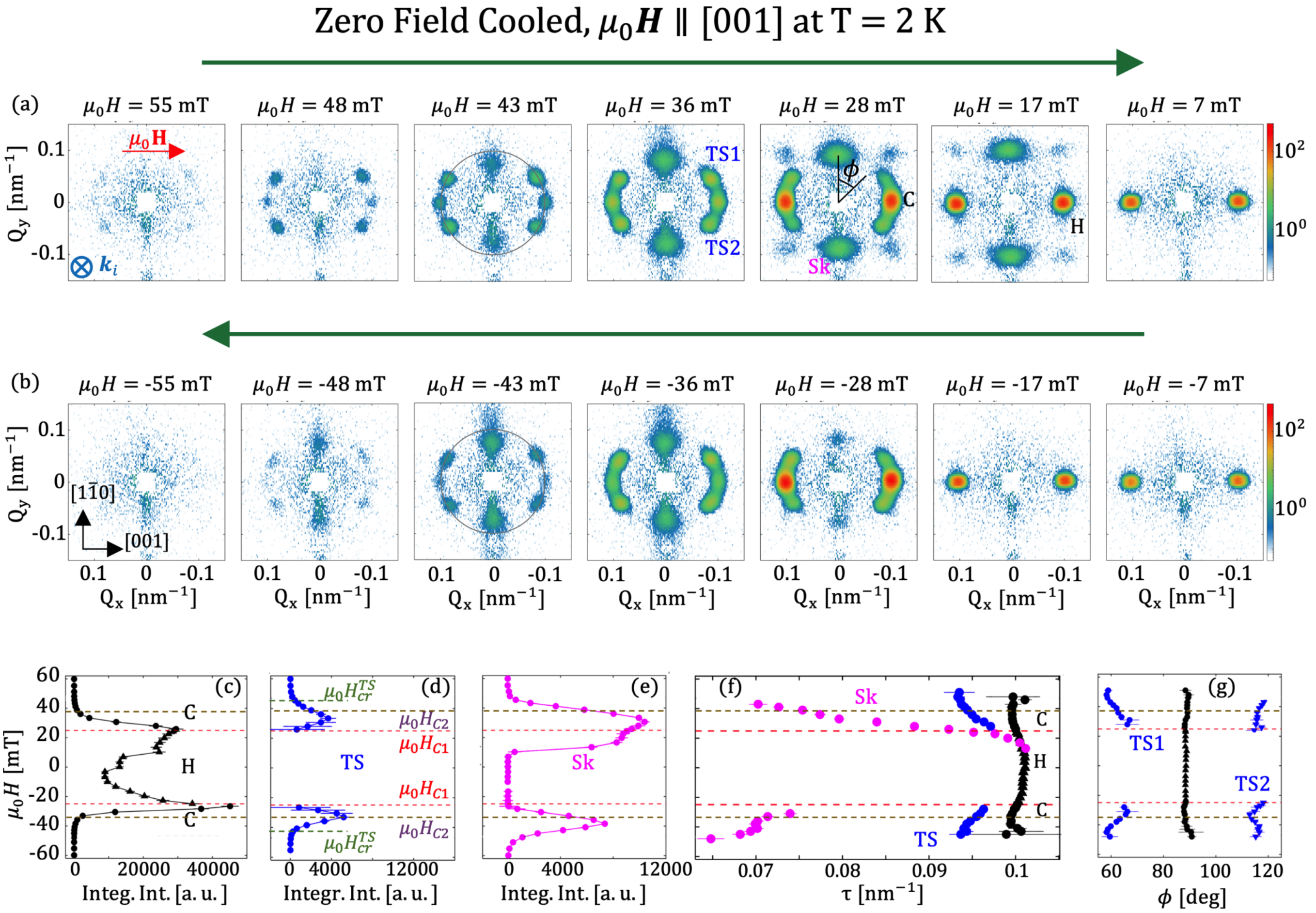

FIG. 2. (a), (b) Show SANS patterns recorded at $T = 2$ K for selected fields using the protocol schematically depicted in Fig. 1. The arrows above the SANS patterns indicate the direction of change of the magnetic field. The red arrow in the $\mu_0 H = 57$ mT panel indicates the direction of the applied magnetic field, while k_i indicates the direction of the incoming neutron beam. The field dependence of the integrated intensities of the conical (C) and helical (H), TS, and skyrmion peaks are shown in (c), (d), and (e), respectively. The corresponding values of τ are provided in (f), and (g) shows the azimuthal position of the conical and helical and TS Bragg spots. In (c)–(g) the horizontal dashed lines indicate the critical fields $\mu_0 H_{C1}$ and $\mu_0 H_{C2}$, respectively. The green dashed lines in (d) stand for $\mu_0 H_{cr}^{\mathrm{TS}}$.

III. EXPERIMENTAL RESULTS

Figures 2 and 3 show SANS patterns collected for $\mu_0\mathbf{H} \parallel [001]$ at $T = 2$ and 18 K, respectively, following the measurement procedure illustrated by Fig, 1(b) (for other temperatures the reader is referred to the Appendix, Figs. 9–11). In these figures, the upper rows [respective panels (a)] show SANS patterns recorded by reducing the magnetic field from well above $\mu_0 H_{C2}$ to zero. The direction of the magnetic field was subsequently reversed and the patterns of the middle rows [respective panels (b)] were recorded for negative fields. The sequence of the magnetic field change is illustrated by the green arrows above the corresponding SANS patterns and for the sake of comparison, patterns measured for positive magnetic fields are shown above the corresponding pattern for negative fields. This representation highlights the impact of the direction of change of the magnetic field on the observed behavior. A comparison of Figs. 2 and 3 shows that at $T = 2$ K and at intermediate field strengths the SANS patterns strongly depend on the magnetic field sign whereas this effect vanishes at $T = 18$ K.

Panels (c), (d), and (e) of Figs. 2 and 3 show the integrated intensities of the conical and helical, tilted spiral, and skyrmionic states, deduced from the fitting each scattering spot/peak by a Gaussian function. This fit also provides the characteristic wave numbers $\tau = 2\pi/L_D$, with L_D the periodicity of the respective modulations, depicted in (f), as well as the tilting angle of the TS state, reported in (g).

The moduli of the critical fields $\mu_0 H_{C2}$ and $\mu_0 H_{cr}^{\mathrm{TS}}$ of the transition between the field-polarized state on one side and the conical and tilted spiral states on the other side, are estimated from the respective integrated intensities. Within the experimental accuracy these fields correspond to the turning point (ideally the maximum of the second derivative) of the intensity versus magnetic field curves. At 2 K the values of both $\mu_0 H_{C2}$ and $\mu_0 H_{cr}^{\mathrm{TS}}$ are about 10% higher for the positive than for the negative fields. These differences, which are characteristic of first-order transitions, decrease with increasing temperature and vanish above ∼20 K.

We will in the following look more closely to the evolution of the scattering at $T = 2$ K. The patterns collected for high and low fields do not depend on the direction of the magnetic

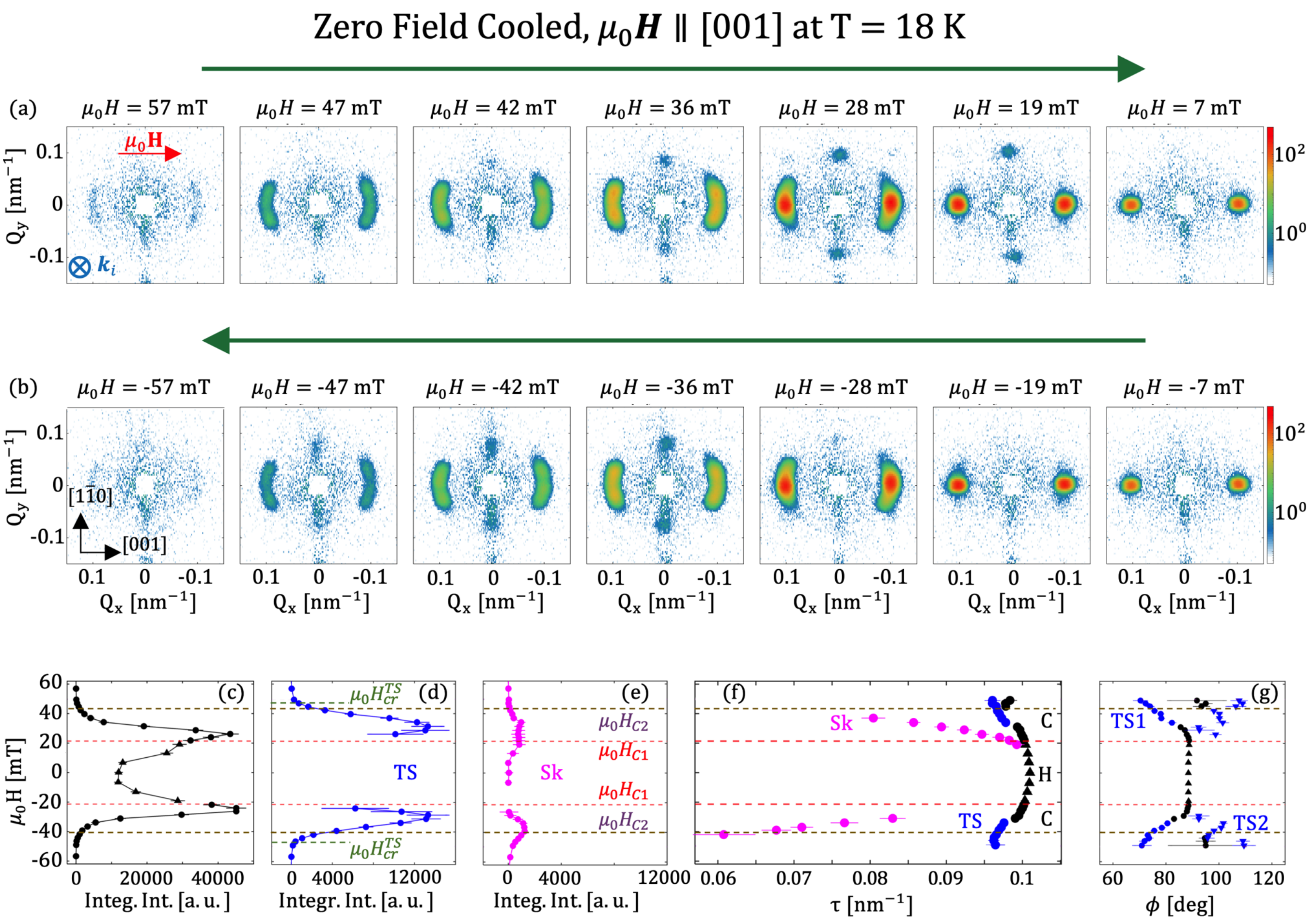

FIG. 3. (a), (b) Show SANS patterns recorded at $T = 18$ K for selected fields using the protocol schematically depicted in Fig. 1. The arrows above the SANS patterns indicate the direction of change of the magnetic field. The red arrow in the $\mu_0H = 57$ mT panel indicates the direction of the applied magnetic field, while k_i the direction of the incoming neutron beam. The field dependency of the integrated intensities of the conical (C) and helical (H), TS, and skyrmion peaks are shown in (c), (d), and (e), respectively. The corresponding values of the characteristic wave numbers τ are provided in (f), and (g) shows the azimuthal position of the conical and helical and TS peaks. In (c)–(g) the horizontal dashed lines indicate the critical fields μ_0H_{C1} and μ_0H_{C2}, respectively. The green dashed lines in (d) stand for $\mu_0H^{\mathrm{TS}}_{cr}$.

field. At the high-field limit, for $\mu_0H = \pm 55$ mT, the modulus of the magnetic field exceeds μ_0H_{C2}, driving the system to the field-polarized state, where the magnetic moments are aligned along the magnetic field and the SANS intensity vanishes. At the low-field limit, where $\mu_0H = \pm 7$ mT, the magnetic field modulus is less than μ_0H_{C1}. Thus, the SANS patterns correspond to the helical state, where the spirals are oriented along the equivalent ⟨001⟩ directions imposed by cubic anisotropy. For the specific sample orientation, only the helical domains aligned along [001] produce scattering, seen as two Bragg peaks in the horizontal direction. In this configuration the Bragg peaks of the helical (e.g., at $\mu_0H = 0$) and the conical states appear at the same positions on the detector and cannot be distinguished from each other. In the intermediate magnetic field region, with $\mu_0H_{C1} \lesssim |\mu_0H| \lesssim \mu_0H_{C2}$, additional intensity appears besides the conical Bragg peaks, indicating the skyrmionic (Sk) and tilted spiral (TS) scattering. The former is confined in the plane perpendicular to $\mu_0\mathbf{H}$ and appears as two spots along $[1\bar{1}0]$, while the latter consists of four Bragg spots, two around each conical Bragg peak position, from which they are separated by a tilting angle $\alpha = \Delta\phi$, with ϕ the azimuthal angle. The TS state is almost unaffected by the change of direction of the applied magnetic fields, while both the conical and skyrmionic states are strongly affected by it. This effect can be observed in the integrated intensities reported in (c), (d), and (e) of Figs. 2 and 3 for the conical and helical, TS, and LTS states.

The integrated intensity of the conical peaks is higher for the negative magnetic fields than for the corresponding positive fields. This disparity is due to the different profiles of the rocking curves, that could not be fully probed because of the limited rocking curve measurement range discussed before. Moreover, a small shift of the rocking curves' center was observed between positive and negative fields. In combination with the wide profile of the rocking curves, this could partially explain the observed intensity differences.

As shown in Fig. 2(d), the tilted spiral scattering appears around μ_0H_{C2}, the intensity increases as the magnetic field is decreased, peaks just before μ_0H_{C1}, and then decreases sharply and disappears at μ_0H_{C1}. The tilted spiral intensity is recovered when reversing the magnetic field. This scattering thus does not depend on the magnetic history, in contrast, to the intensity of the skyrmionic scattering, shown in Fig. 2(e). With decreasing the magnetic field, the skyrmionic scattering appears just below $\mu_0 H_{C2}$, reaches its maximum value around $\mu_0 H_{C1}$, and persists even in the helical state, where the intensity decays and disappears just before reaching $\mu_0 H =$ 0 mT. However, when the field direction is inverted, this scattering emerges only after crossing $-\mu_0 H_{C1}$ and almost together with the TS peaks. Like all other contributions, this scattering also disappears as $-\mu_0 H_{C2}$ is approached.

The changes in the scattering discussed above also affect the characteristic wave numbers of the modulations. Near $\mu_0 H_{C2}$, as the field decreases following the measurement procedure discussed before, the wave number of the conical scattering, shown in Fig. 2(f), first slightly decreases and then increases reaching its maximum value of $10.11(1) \times 10^{-4}$ nm^{-1} at $\mu_0 H = 0$ mT. A symmetrical behavior is observed when the magnetic field direction is inverted and the field intensity increased. Similar values and a similar symmetrical behavior, with respect to the magnetic field direction, are also found for the wave number of the tilted spiral scattering. Also, this wave number increases with decreasing field intensity from $9.34(2) \times 10^{-4}$ nm^{-1} at $\mu_0 H_{C2}$ to $9.78(1) \times 10^{-4}$ nm^{-1} at $\mu_0 H_{C1}$ where it reaches its maximum. The wave numbers of the skyrmionic scattering are significantly lower than those of the other two contributions, as seen, e.g., in the SANS patterns for $\mu_0 H = \pm 43$ mT. At high positive magnetic fields we find values as low as $7.63(6) \times 10^{-4}$ nm^{-1} which, however, quickly increase with decreasing field, tending towards the wave numbers of the other contributions and reaching a maximum of $9.98(6) \times 10^{-4}$ nm^{-1} at $\mu_0 H =$ 13 mT. As the field direction is inverted, and the skyrmionic scattering reappears just below $|\mu_0 H_{C1}|$, its wave number takes values comparable, and even lower, to those found for high positive fields.

Finally, Fig. 2(h) depicts the field dependency of the azimuthal position of the tilted spiral and conical peaks. The latter remain in the same angular position, at ≈90°, for all magnetic fields. At the same time, with decreasing the intensity of the magnetic field, the position of the TS peaks oscillates and drifts towards the position of the conical and helical peaks. However, these peaks do not merge with the conical peaks but disappear abruptly at $|\mu_0 H_{C1}|$, indicating a discontinuous transition.

The same measurements have been performed at different temperatures, and the effect of increasing temperature becomes visible at the scattering patterns obtained for $T = 18$ K shown in Fig. 3. At this temperature the skyrmionic scattering is considerably weaker than at $T = 2$ K. At the same time the tilted spiral peaks almost merge with the conical ones and their discrimination becomes difficult, which affects the resulting integrated intensities displayed in Figs. 3(a) and 3(b), as well as the deduced azimuthal angles shown in 3(h). At this temperature, the effect of magnetic history on the SANS patterns is almost negligible with the exception of the skyrmionic scattering, which appears over a narrower magnetic field range than at 2 K, as shown in Fig. 3(c), and does not persist into the helical phase when the magnetic field is decreased from $\mu_0 H_{C2}$ down to zero. On the other hand, the wave numbers of the different contributions to the scattering and their magnetic field dependence, shown in Figs. 3(d) and 3(e), are very similar to those found at 2 K.

The most striking difference between 2 and 18 K is in the magnetic field dependence of the azimuthal position of the tilted spiral scattering depicted in Fig. 3(h). Despite the difficulty in discriminating the peaks, there is a clear indication for a gradual merging of the tilted spiral and conical and helical spots with decreasing $|\mu_0 H|$, in contrast to the abrupt change found at 2 K. The way the tilted spiral peaks emerge out of the conical and helical scattering as a function of magnetic field and temperature is illustrated in the contour plots of the scattered intensity versus magnetic field and azimuthal angle shown in Fig. 4. At $T = 2$ K the tilted spiral scattering appears in an abrupt, stepwise, manner and is well separated from the conical and helical peaks that are centered at $\phi = 0°$ and 180°. As the temperature increases, the angular separation between the conical and helical and the tilted spiral peaks decreases and the transition becomes gradual. Already at 18 K it is almost impossible to separate the peaks from each other and at higher temperatures the tilted spiral phase appears as a broadening of the helical and conical peaks, an effect that spans the whole conical phase and persists up to above 35 K (see Appendix, Fig. 12), the highest temperature where our measurements have been performed.

Figure 5 shows the contour plots of the intensities deduced from our fits: the conical intensity (along [001]) is shown in Fig. 5(a) and vanishes above $\mu_0 H_{C2}$. The TS intensity shown in Fig. 5(b) persists slightly above the $\mu_0 H_{C2}$ and disappears for field intensities lower than $\mu_0 H_{C1}$. The patterned area in this panel identifies the region where it was impossible to distinguish between the conical and TS states. The magnetic field and temperature dependence of the skyrmionic intensity are shown in Fig. 5(c). This intensity is more extended in the positive field region, where it is present also below $\mu_0 H_{C1}$, compared to the negative fields, where it appears confined between $-\mu_0 H_{C1}$ and $-\mu_0 H_{C2}$. This highlights the highly hysteretic behavior of this scattering.

IV. PHENOMENOLOGICAL MODEL

In the following we discuss these results in the frame of the phenomenological theory introduced by Dzyaloshinskii [31]. The magnetic energy density of a bulk noncentrosymmetric ferromagnet with spatially dependent magnetization vector $\mathbf{M}$ can be written as

$$W_0(\mathbf{m}) = A \sum_{i,j} \left(\frac{\partial m_j}{\partial x_i} \right)^2 + D\, w_D(\mathbf{m}) - \mu_0 M_0 \mathbf{m} \cdot \mathbf{H}, \quad (1)$$

where A and D are the coefficients of the exchange and Dzyaloshinskii-Moriya interactions, respectively; $\mathbf{m} = \mathbf{M}/M_0 = (\sin\theta\, \cos\psi; \sin\theta\, \sin\psi; \cos\theta)$ with $M_0 = 111.348$ kA/m the saturation magnetization at $T = 0$ K; $\mathbf{H} = (0, 0, H)$ is the applied magnetic field and x_i are the Cartesian components of the spatial variable. We will also express our results as a function of the reduced magnetic field $\mathbf{h} = \mathbf{H}/H_D$ with $\mu_0 H_D = D^2/(AM)$.

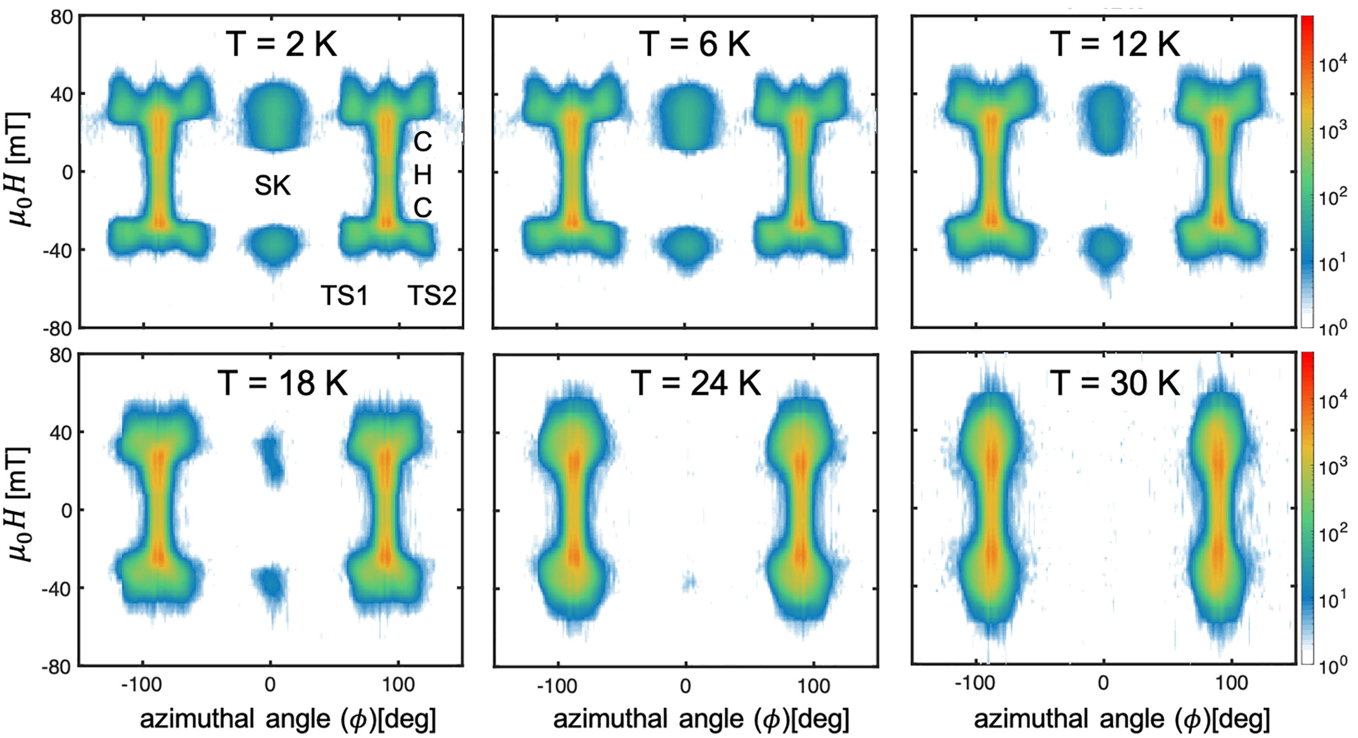

FIG. 4. Contour plots of the scattered intensity recorded between $Q = 0.05$ and 0.013 nm^{-1} as a function of the polar angle ϕ and the magnetic field for the temperatures, where measurements were performed.

The functional w_D is composed of Lifshitz invariants $\mathcal{L}_{i,j}^{(k)} = m_i \partial m_j/\partial x_k - m_j \partial m_i/\partial x_k$ that are energy terms involving first derivatives of the magnetization with respect to the reduced spatial coordinates (normalized to the lattice constant a). Consequently, the sign of D determines the sense of the magnetization rotation.

$W_0(\mathbf{m})$ includes only basic interactions essential to stabilize skyrmion and helical states and specifies their most general features attributed to all chiral ferromagnets. Our calculations are performed for cubic helimagnets with $w_D = \mathbf{m} \cdot \nabla \times \mathbf{m}$. However, the results are of more general validity and may be applied to magnets with other symmetry classes [21] including different combinations of Lifshitz invariants.

For cubic helimagnets, the isotropic energy density given by Eq. (1) is usually supplemented by the exchange and cubic anisotropic contributions [5,30]

$$\Phi_a = b_{ea}(T) \sum_i (\partial m_i/\partial x_i)^2 + k_c(T) \sum_i m_i^4, \qquad (2)$$

where $b_{ea} = B_{ea}/A$ and $k_c = K_c A/D^2$ are the reduced exchange and cubic anisotropy constants, respectively, which are in general temperature dependent. The constants k_c and b_{ea} are typically one order of magnitude smaller than the exchange stiffness A. Nevertheless, they play an important role in the stabilization and control of tilted spiral states. Furthermore, the cubic anisotropy can explain the stability of the low-temperature skyrmion phase in $\mathrm{Cu_2OSeO_3}$ [29].

For a more direct comparison between experiment and theory we will in the following discuss the results of simulations obtained for $k_c > 0$ with easy $\langle 001 \rangle$ axes, which correspond to the case of $\mathrm{Cu_2OSeO_3}$), and $b_{ea} < 0$ with easy $\langle 111 \rangle$ axes. Details on the energy minimization procedure are provided in the Appendix.

In our model the tilted spiral state is found only for $\mathbf{h} \parallel \langle 001 \rangle$, in agreement with experiment. Figures 6(b) and 6(c) show color plots of the m_y magnetization component in both conical and tilted spirals. The dependence of the spiral energy on the tilt angle α with the spiral propagation vector $\mathbf{Q}$ varying in the $(1\bar{1}0)$ plane is shown in Figs. 6(d) and 6(e) for two sets of anisotropy constants and for several field values: 6(d) $k_c = 0.1$, $b_{ea} = -0.1$; 6(e) $k_c = 0.15$, $b_{ea} = -0.15$. In the first case, for $k_c = 0.1$ in Fig. 6(d), $\mathbf{Q}$ smoothly moves out of the field direction. Indeed, the energy difference between the conical state (energy maximum) and a tilted spiral (energy minimum) is very small, and the energy curve exhibits a plateaulike behavior over the whole range where a tilted spiral can be stabilized.

For a higher cubic anisotropy, $k_c = 0.15$ in Fig. 6(e), however, there is a small energy barrier between the conical and the tilted spirals (dotted line corresponding to $h = 0.175$), which would lead to an abrupt change of the spiral wave vector. Also in this case the energy minimum corresponding to a tilted spiral is quite pronounced and develops within a rather restricted field range from 0.17 to 0.18.

In view of these results the behavior of $\mathrm{Cu_2OSeO_3}$, as shown in Fig. 4, would indicate a temperature dependent k_c, the strength of which would decrease with increasing temperature.

V. QUALITATIVE MODEL FOR $\mathrm{Cu_2OSeO_3}$

For a more quantitative comparison of the model and the experimental findings it is important to determine the

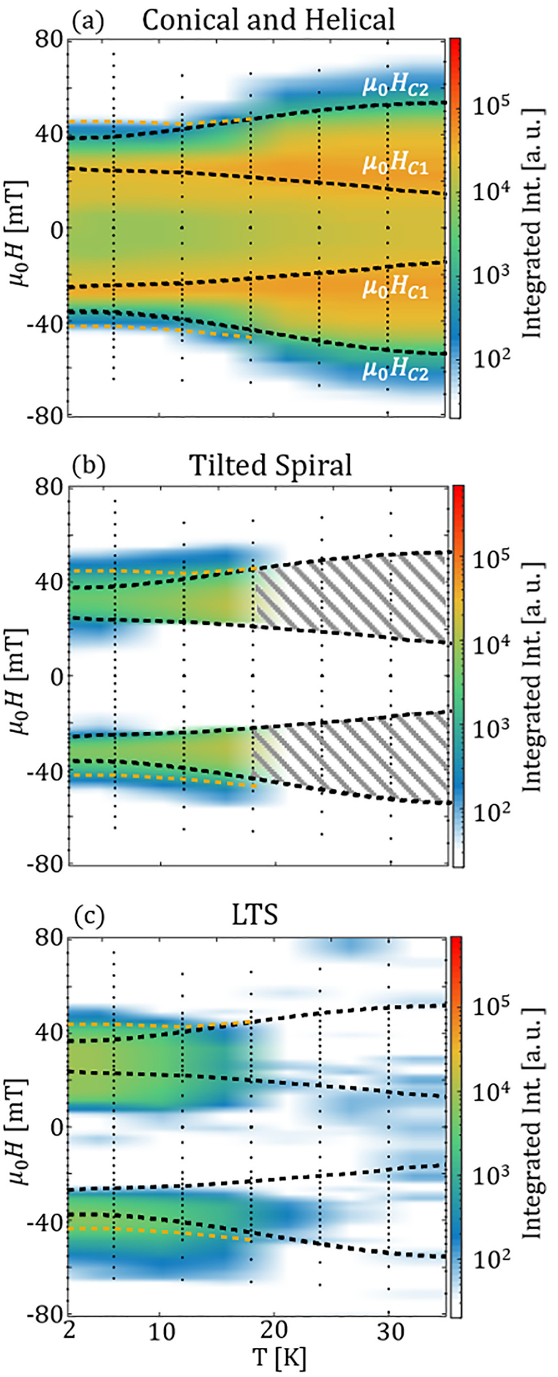

FIG. 5. (a)–(c) Contour plots of the intensities of the conical, tilted spiral, and low-temperature skyrmionic scattering for $\mathbf{H} \parallel [001]$. The black dots indicate the H-T points at which the measurements were performed. The patterned area in (b) shows the temperature and field region where the we observe a broadening of the conical peaks and we cannot unambiguously discriminate the TS from the conical peaks. The black and orange dotted lines indicate $\mu_0 H_{C2}$ and $\mu_0 H_{cr}$, respectively.

constants in Eqs. (1) and (2). For the most important Heisenberg exchange and Dzyaloshinskii-Moriya interactions, $A = -k_B J/a$ and $D = k_B D_{DM}/a^2$, with $a = 0.891\,113$ nm the lattice constant, we adopt the values evaluated in Ref. [30], where $J = -11.19$ K and $D_{\mathrm{DM}} = -2.46$ K were determined using *ab initio* density functional theory calculations.

The important obstacle, however, lies in the determination of the dimensionless anisotropy constants k_c and b_{ea}, as they usually appear together in the magnetization processes and exhibit pronounced temperature dependencies.

In the following, we discuss a strategy that can lead to a complete quantitative model for $\mathrm{Cu_2OSeO_3}$. Figure 7(b) shows that for a weak cubic anisotropy, e.g., for $k_c = 0.05$, and for sufficiently high values of $|b_{ea}|$ there is an abrupt transition between the conical phase, where $\alpha = 0$ and the tilted spiral phase, where spirals orient along $\langle 111 \rangle$. At a higher value of $k_c = 0.1$ and with increasing h [Fig. 7(c)] α first increases reaching a maximal value of $\alpha_{\max}$ before subsequently decreasing back to zero. The value of $\alpha_{\max}$ depends on the ratio of the competing fourth-order cubic and exchange anisotropies, and it is depicted in Fig. 7(g). As the modulus of exchange anisotropy increases above the critical value of 0.14, the TS state is stabilized even at zero magnetic field.

By further increasing k_c to 0.15, a qualitatively different behavior sets in as shown in Fig. 7(d). In this case with increasing magnetic field $\mathbf{Q}$ first jumps abruptly to a rather high angle value of α, about 35° for $b_{ea} = -0.15$, and then stays almost unchanged, forming a plateau, up to the critical field of the first-order phase transition to the field-polarized state. This behavior occurs even when the modulus of b_{ea} is smaller than that of k_c, e.g., for $b_{ea} = -0.05$. Furthermore, when plotting $\alpha_{\max}$ as a function of b_{ea} for fixed k_c [see Fig. 7(g)] we find another extended plateau connecting the conical phase for low moduli of b_{ea} and the tilted spiral (along $\langle 111 \rangle$) for high moduli of b_{ea}.

Figure 7(e) shows the stability areas of the conical and tilted spirals for each value of the cubic anisotropy. The dotted lines indicate h_{C2}, the field of the first-order phase transition between the conical and the field-polarized state, which decreases substantially with increasing k_c. This figure illustrates the strong dependence of the field range Δh^{TS}, over which the TS is stabilized, on both k_c and b_{ea}. This is also highlighted in Fig. 7(f), which depicts the ratio $\Delta h^{\mathrm{TS}}/h_{C2}$. Both figures reveal that for $k_c < 0.1$ the upper critical field of the TS phase h_{cr}^{TS} remains below h_{C2}. For higher values of k_c, however, h_{cr}^{TS} increases and even exceeds h_{C2}. Thus, for the highest moduli of b_{ea}, for which the lower critical field of the TS phase vanishes, the ratio $\Delta h^{\mathrm{TS}}/h_{C2}$ may become higher than 1. This is barely noticeable for $k_c = 0.1$ but becomes prominent for $k_c = 0.15$. The tilted spiral can therefore transit into the field-polarized state at higher fields than the conical state, in agreement with our experimental observations for $T < 18$ K (Figs. 2, 3, 5, and 8).

A similar change of behavior with increasing k_c is also found for the maximum tilt angles $\alpha_{\max}$. As shown in Fig. 7(g), $\alpha_{\max}$ strongly increases with increasing b_{ea}. However, for $k_c = 0.15$ this increase levels off around $\alpha_{\max} \sim 30°$, an effect that becomes less and less visible with increasing k_c and disappears at a critical value of $k_{c,cr} \sim 0.06$ (see Fig. 13). For $k_c < k_{c,cr}$ one observes just a jump between the two angles that correspond to the $\langle 001 \rangle$ and $\langle 111 \rangle$ crystallographic axes.

These results lead to the conclusion that $k_{c,cr}$ separates a regime of weak cubic anisotropy (for $k_c < k_{c,cr}$), where tilted spirals are experimentally barely distinguishable from

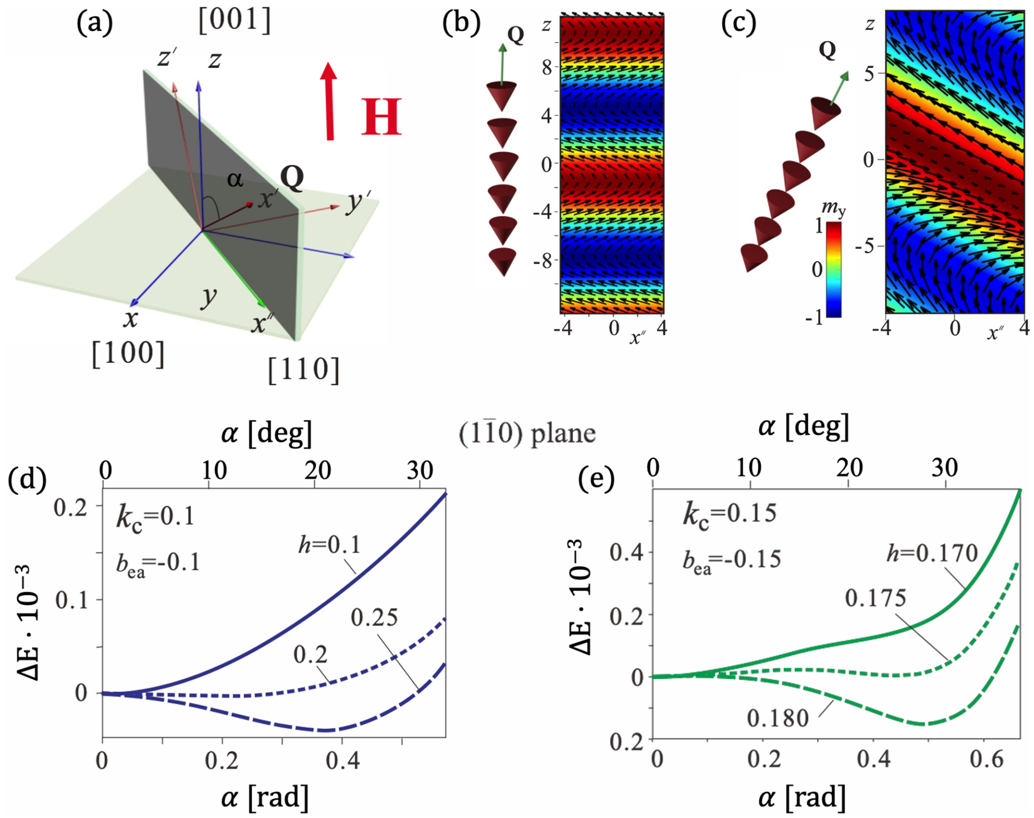

FIG. 6. (a) Schematics of a coordinate system used in our numerical search for two-dimensional tilted spiral states. The energy density is written in the coordinate system (x', y', and z') and is minimized with respect to the angle α. (b), (c) Depict sketches of the one-dimensional spiral states, cones (b) and tilted spirals (c), as well as the corresponding contour plots of the component m_y of the magnetization vector, evaluated in the coordinate system (x, y, z). (d), (e) Show the energy density plotted as a function of the tilt angle α in the $(1\bar{1}0)$ plane for two representative sets of the anisotropy coefficients [(d) $k_c = 0.1$, $b_{ea} = -0.1$; (e) $k_c = 0.15$, $b_ea = -0.15$] and for several field values highlighting the transition into the tilted spiral state.

the cones, from another one of strong cubic anisotropy (for $k_c > k_{c,cr}$) characterized by well-defined tilted spirals, which appear abruptly out of the conical state and persist even above h_{C2}. We can thus explain the observed change of behavior around 18 K by the change from weak to strong cubic anisotropy regimes. As the nucleation of skyrmions is assumed to be related to the stability of tilted spirals [27,29,32], this change of behavior around 18 K would explain the increased stability of skyrmions at low temperatures.

Further comparison between model and experiment at low temperatures leads to the following conclusions: (i) A value of $\alpha_{\max} \approx 34^\circ$, as observed experimentally at 2 K, cannot be reached for $k_c = 0.1$ because in that case with increasing $|b_{ea}|$ the spirals would jump towards the $\langle 111 \rangle$ directions before reaching this angle. On the other hand, for $k_c = 0.15$ this angle is readily obtained and with a weak, plateaulike field dependence for $b_{ea} = -0.15$. (ii) At low temperatures, our experimental results show that the TS phase sets in over a magnetic field interval $\Delta h^{\mathrm{TS}}/h_{C2} \approx 0.59$ which, as shown in Fig. 7(f), leads to $b_{ea} \approx -0.18$, which is consistent with the estimated value for Zn-doped Cu_2OSeO_3 [33]. (iii) The relative difference $\delta = (h_{cr}^{\mathrm{TS}} - h_{C2})/h_{C2}$ is an additional parameter that can be compared with experiment. However, as mentioned above, the experimental values of both critical fields $\mu_0 H_{C2}$ and $\mu_0 H_{cr}^{\mathrm{TS}}$ depend strongly on the magnetic history. At $T = 2$ K, we find $\delta \sim 22\%$ and $\sim 25\%$ for positive and negative fields, respectively, a value substantially higher than $\sim 2\%$ derived from our numerical simulations. Furthermore, the difference between $\mu_0 H_{C2}$ and $\mu_0 H_{cr}^{\mathrm{TS}}$ persists even at $T = 18$ K (see Figs. 3 and 8), where we find $\delta \sim 10$ % and ~ 17 % for positive and negative fields, respectively. This hysteretic behavior reflects the presence of potential barriers and the first-order character of the phase transitions at h_{C2} and h_{cr}^{TS}, respectively, and could be at the origin of the discrepancies in the values of δ between model and experiment.

Our theoretical results for $k_c = 0.15$ explain qualitatively the following experimental observations at $T = 2$ K: (i) The first-order phase transitions to the field-polarized state. The first-order nature of these transitions is confirmed by the coexistence of conical and tilted spiral states and the asymmetry in the moduli of $\mu_0 H_{C2}$ and $\mu_0 H_{cr}^{\mathrm{TS}}$ between positive and negative fields. (ii) The abrupt appearance of the tilted spiral state. (iii) The values of the angles and the magnetic field intervals over which the spiral canting sets in. We note that the value of $k_c = 0.15$ exceeds by a factor of 2 the value of $k_c = 0.07$ estimated by [28] from a comparison between experiment and a model similar to ours but which included dipole interactions and discarded exchange anisotropy.

With increasing temperature towards 18 K, k_c decreases and the first-order phase transition between the tilted spiral

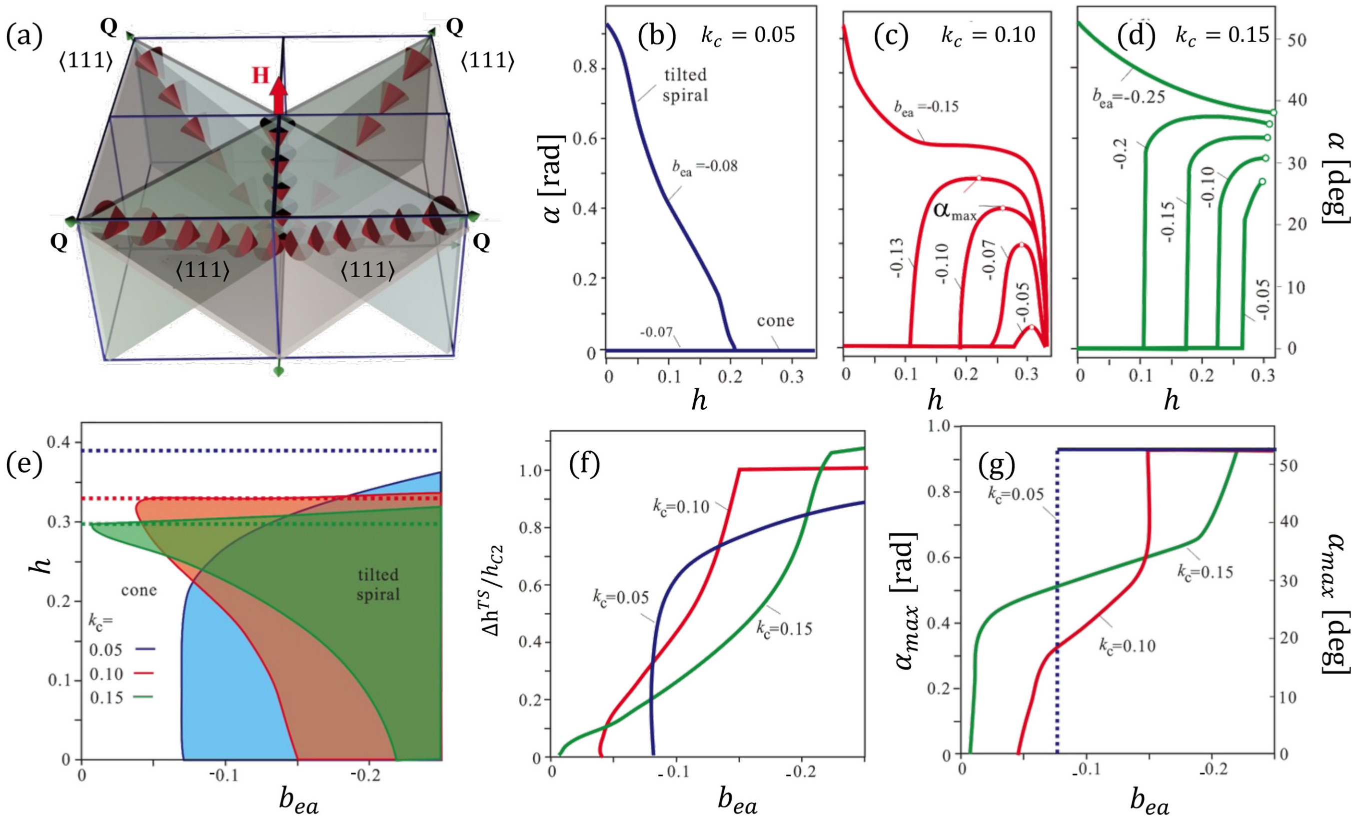

FIG. 7. Results obtained for **H** ∥ [**001**]. (a) Schematics of coexisting conical and tilted spiral states consisting of four energetically equivalent domains canting towards the ⟨111⟩ directions. The magnetic field dependence of the tilt angle α is shown in (b), (c), and (d) for cubic anisotropy values of $k_c = 0.05$, 0.10, and 0.15, respectively, and for selected values of the exchange anisotropy b_{ea}. In (c), the tilted spiral almost returns back to the direction of the field, whereas in (d) the spiral is deflected from the field by quite a large angle α and undergoes a first-order phase transition to the field-polarized homogeneous state. For the same values of k_c (e) shows a diagram depicting the stability regions of the the conical and TS states. The dotted lines indicate h_{C2}, which decreases with increasing k_c. The lines are colored according to the cubic anisotropy value just like the stability regions of the TS phase. The field range Δh^{TS}, over which the TS is stabilized, varies strongly with both k_c and b_{ea}. The ratio $\Delta h^{\mathrm{TS}}/h_{C2}$ as well as the maximum tilt angle $\alpha_{\max}$ are plotted as a function of b_{ea} in (f) and (g), respectively.

and the field-polarized state becomes less obvious because with increasing field the spirals smoothly slant away from the cones and almost return back to them close to h_{C2}. Such a behavior would correspond to $k_c = 0.1$. As mentioned above, this decrease of k_c is consistent with the increase of the experimentally observed values of $\mu_0 H_{C2}$. The ratio between the $\mu_0 H_{C2}$ values at $T = 18$ and 2 K is about 1.3 and 1.2 for positive and negative fields, respectively. Thus, if $k_c = 0.15$ for $T = 2$ K, the corresponding value at $T = 18$ K would be equal to $k_{c,cr} = 0.06$. The behavior experimentally observed for $T > 18$ K would therefore correspond to $k_c < k_{c,cr}$. However, as in the latter case the TS state does occur at zero field, we deduce that $b_{ea} > -0.08$.

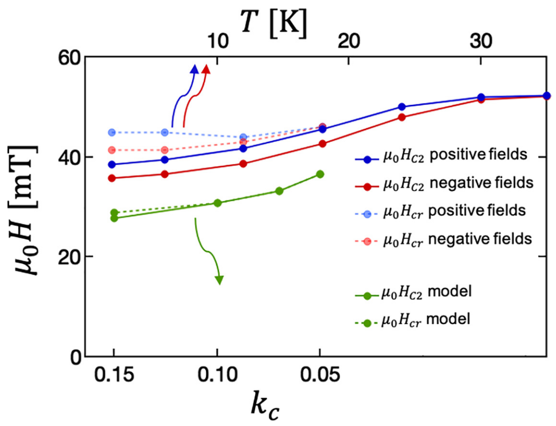

FIG. 8. Experimental and theoretical (absolute) values of $\mu_0 H_{C2}$ and $\mu_0 H_{cr}$ plotted as a function of temperature (top axis) and k_c (bottom axis), respectively. The blue and red data represent the experimental values determined for positive (i.e., for decreasing magnetic field strength) and negative (i.e., for increasing magnetic field strength) fields, respectively.

Our model thus captures the main features of the low-temperature behavior of Cu_2OSeO_3. This is illustrated by Fig. 8, which depicts the (absolute) values of $\mu_0 H_{C2}$ and $\mu_0 H_{cr}$, plotted as a function of temperature and k_c for the experimental and theoretical values, respectively.

A subsequent endeavor would be to construct a fully quantitative model for a bulk helimagnet Cu_2OSeO_3 by taking into account experimental data for other field directions and possibly including dipole-dipole interactions. These have been considered by [27,28] as demagnetizing corrections are important in Cu_2OSeO_3. On the other hand, the phenomena we are discussing here have been reported consistently in the literature for different samples and with different shapes [26–29]. In addition, the temperature dependence of the magnetization below 30 K is very weak [26,34] in contrast to the observed change in behavior in the same temperature range. We have therefore disregarded these interactions in our model and used this conventional approximation to accelerate the minimization procedure for all states considered here.

VI. CONCLUSIONS

Our in-depth investigation by small-angle neutron scattering and numerical simulations of Cu_2OSeO_3 reveals an unconventional temperature dependence of the magnetic phase diagram when the magnetic field is applied along $\langle 001 \rangle$. At low temperatures, e.g., $T = 2$ K, the tilted spiral scattering appears in an abrupt, stepwise, manner and is well separated from the conical peaks. With increasing temperature, however, the angular separation between the conical and the tilted spiral peaks decreases and at 18 K the transition becomes gradual. Already at 18 K it is almost impossible to separate the tilted spiral from the conical peaks and at higher temperatures the tilted spiral phase appears as a broadening of the helical and conical peaks, an effect that spans the whole conical phase and persists up to 35 K and possibly above. At all temperatures the tilted spiral phase appears between $\mu_0 H_{C2}$ and $\mu_0 H_{C1}$ in contrast to the hysteretic behavior of the skyrmionic scattering, which appears at different regions of the H-T phase diagram depending on magnetic history.

Our theoretical model based on the theory introduced by Dzyaloshinskii captures the main features of the experimental findings, which can be accounted for by the interplay between exchange and cubic anisotropy. In this work, however, we go a step further towards a quantitative comparison between model and experiment and discuss a strategy that leads to an estimate of the anisotropy constants. These are the drivers behind the observed behavior, and their determination is not as trivial as for the interaction constants, that have been obtained either by density functional theory or experimentally. The comparison between model and experiment leads to the conclusion that the anisotropy constants change significantly with temperature and that this temperature dependence explains the change of behavior observed around $T \sim 18$ K, a temperature where a critical value of cubic anisotropy $k_{c,cr} \sim 0.6$ separates two regimes. The high-temperature one ($T > 18$ K) is characterized by weak cubic anisotropy ($k_c < k_{c,cr}$) and encompasses a smooth transition between cones and tilted spirals as well as very weak skyrmionic correlations. In contrast, in the low-temperature regime ($T > 18$ K) a strong cubic anisotropy ($k_c > k_{c,cr}$) induces an abrupt appearance of the tilted spirals and enhances the stability of skyrmions.

The approach we have adopted allows a quantitative comparison between experiment and theory and provides a strategy for an in-depth understanding of chiral magnets in view of tailoring their properties for future applications.

The raw experimental data are available at [35]. Additional data related to this paper may be requested from M.C. [36], C.P. [37], and A.O.L. [38].

ACKNOWLEDGMENTS

The authors are grateful to M. Mostovoy for useful discussions and to the technical staff of ILL for their support during the experiment. A.O.L. thanks U. Nitzsche for technical assistance and acknowledges JSPS Grant-in-Aid (C) No. 21K03406. M.C, A.L., and C.P. acknowledge financial support from the Vrije FOM-programma “Skyrmionics” (Grant No. 838).

APPENDIX

1. Results for other temperatures than those discussed in the main text

Figures 9–11 complement the results shown in Figs. 2–3 and depict the experimentally observed behavior at $T = 6$, 12, and 24 K. Figure 12 shows a contour plot of the scattered intensity as a function of the azimuthal angle ϕ and the magnetic field for $T = 35$ K.

2. Energy minimization

The nonlinear partial differential Euler-Lagrange equations derived from the energy functional have been solved by numerical energy minimization procedure using finite-difference discretization on grids with adjustable grid spacings and periodic boundary conditions. The components of the magnetization vector $\mathbf{m}$ have been evaluated in the knots of the grid, and for the calculation of the energy density we used finite-difference approximation of derivatives with different precision up to eight points as neighbors. Furthermore, in order to check the stability of the numerical routines we additionally refined and coarsened the grids. For axial fields, in order to reduce the artificial anisotropy incurred by the discretization, we used grid spacings $\Delta_y \approx \Delta_x$ leading to grids approximately square in the xy plane. The final equilibrium structure of the modulated states was obtained following an iterative procedure of the energy minimization using simulated annealing and a single-step Monte Carlo dynamics with the Metropolis algorithm. The details of the numerical methods used for the energy minimization are described in, e.g., Ref. [39] and hence will be omitted here.

In order to avoid an impediment introduced by the periodic boundary conditions, which necessarily arises due to the oblique spiral states when using a three-dimensional cube, we performed two-dimensional simulations. For these, we wrote the anisotropy energy density in a coordinate system connected with the wave vector of an oblique spiral and a corresponding plane of rotation. Thus, the axes of the new coordinate system $\acute{z}$ and $\acute{x}$ lie in the plane $(1\bar{1}0)$, and the $\mathbf{Q}$ vector is aligned along $\acute{x}$ and at an angle α from the z axis of an old coordinate system. Consequently, the energy density is minimized with respect to α leading to the optimum value of this angle characterizing the oblique spiral state.

Figure 13 shows complementary results to Fig. 7 revealing the behavior for $k_c = 0.07$.

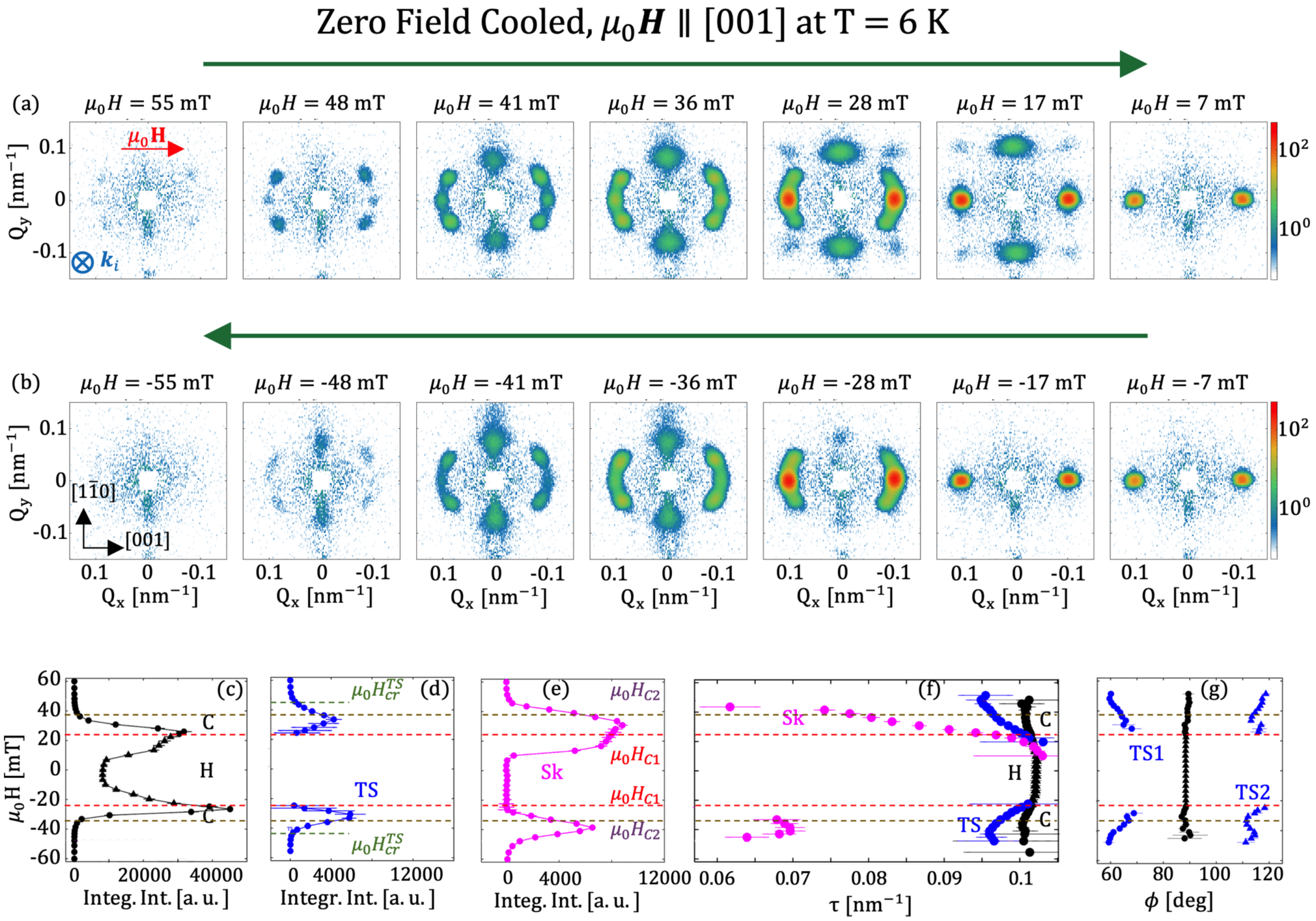

FIG. 9. (a) and (b) show SANS patterns recorded at $T = 6$ K for selected fields using the protocol schematically depicted in Figure 1 of the main text. The arrows above the SANS patterns indicate the direction of change of the magnetic field. The red arrow in the $\mu_0H = 55$ mT panel indicates the direction of the applied magnetic field, while k_i the direction of the incoming neutron beam. The field dependency of the integrated intensities of the conical (C), helical (H), TS and skyrmion peaks are shown in panels (c), (d) and (e), respectively. The corresponding values of the characteristic wavenumbers τ are provided in (f). (g) shows the azimuthal position of the conical/helical and TS peaks. In (c)–(g) the horizontal dashed lines indicate the critical fields μ_0H_{C1} and μ_0H_{C2}, respectively. The green dashed lines in (d) stand for $\mu_0H_{cr}^{\mathrm{TS}}$.

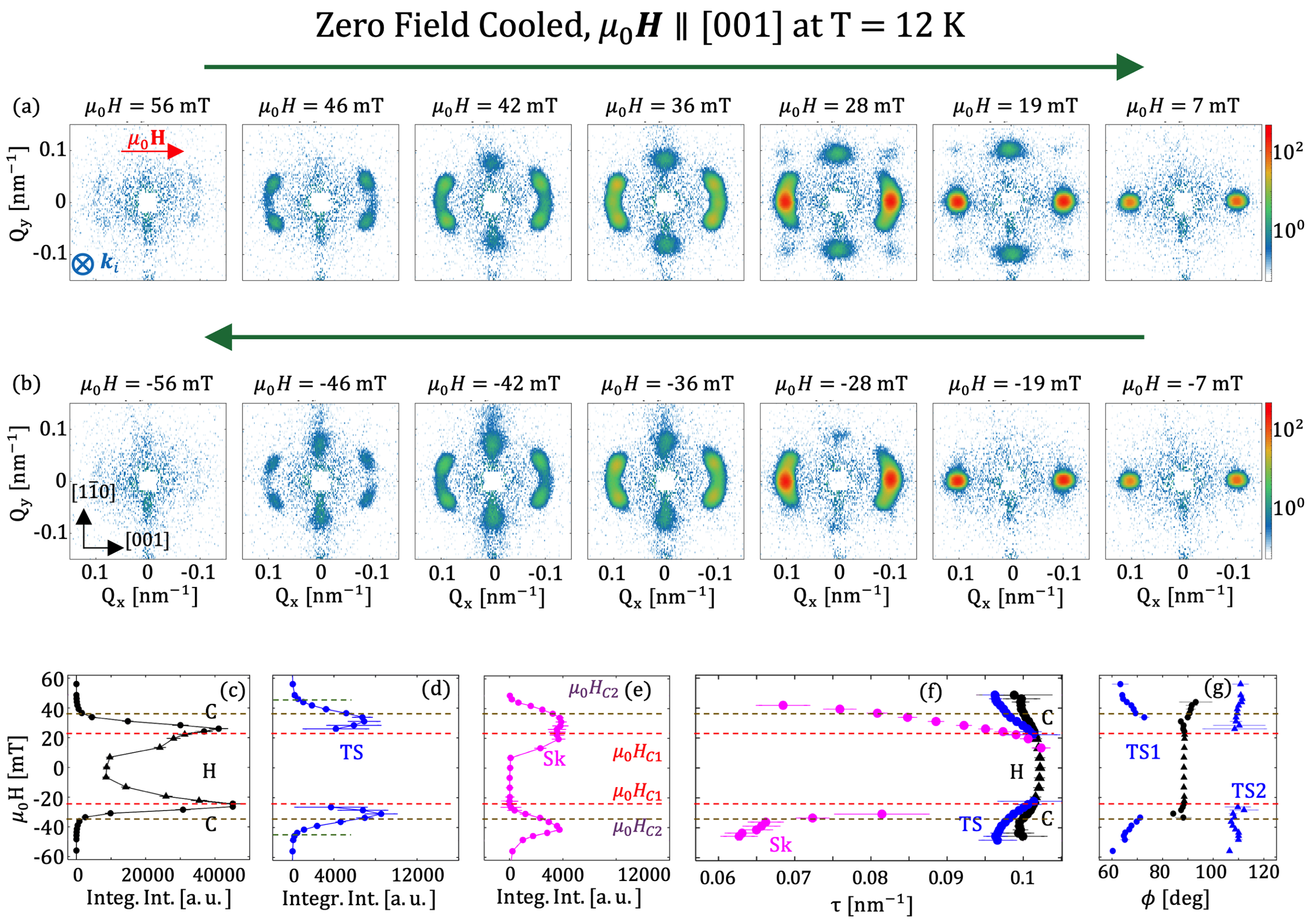

FIG. 10. (a) and (b) show SANS patterns recorded at $T = 12$ K for selected fields using the protocol schematically depicted in Figure 1 of the main text. The arrows above the SANS patterns indicate the direction of change of the magnetic field. The red arrow in the $\mu_0 H = 56$ mT panel indicates the direction of the applied magnetic field, while k_i the direction of the incoming neutron beam. The field dependency of the integrated intensities of the conical (C), helical (H), TS and skyrmion peaks are shown in panels (c), (d) and (e), respectively. The corresponding values of the characteristic wavenumbers τ are provided in (f). (g) shows the azimuthal position of the conical/helical and TS peaks. In (c)–(g) the horizontal dashed lines indicate the critical fields $\mu_0 H_{C1}$ and $\mu_0 H_{C2}$, respectively. The green dashed lines in (d) stand for $\mu_0 H_{cr}^{\mathrm{TS}}$.

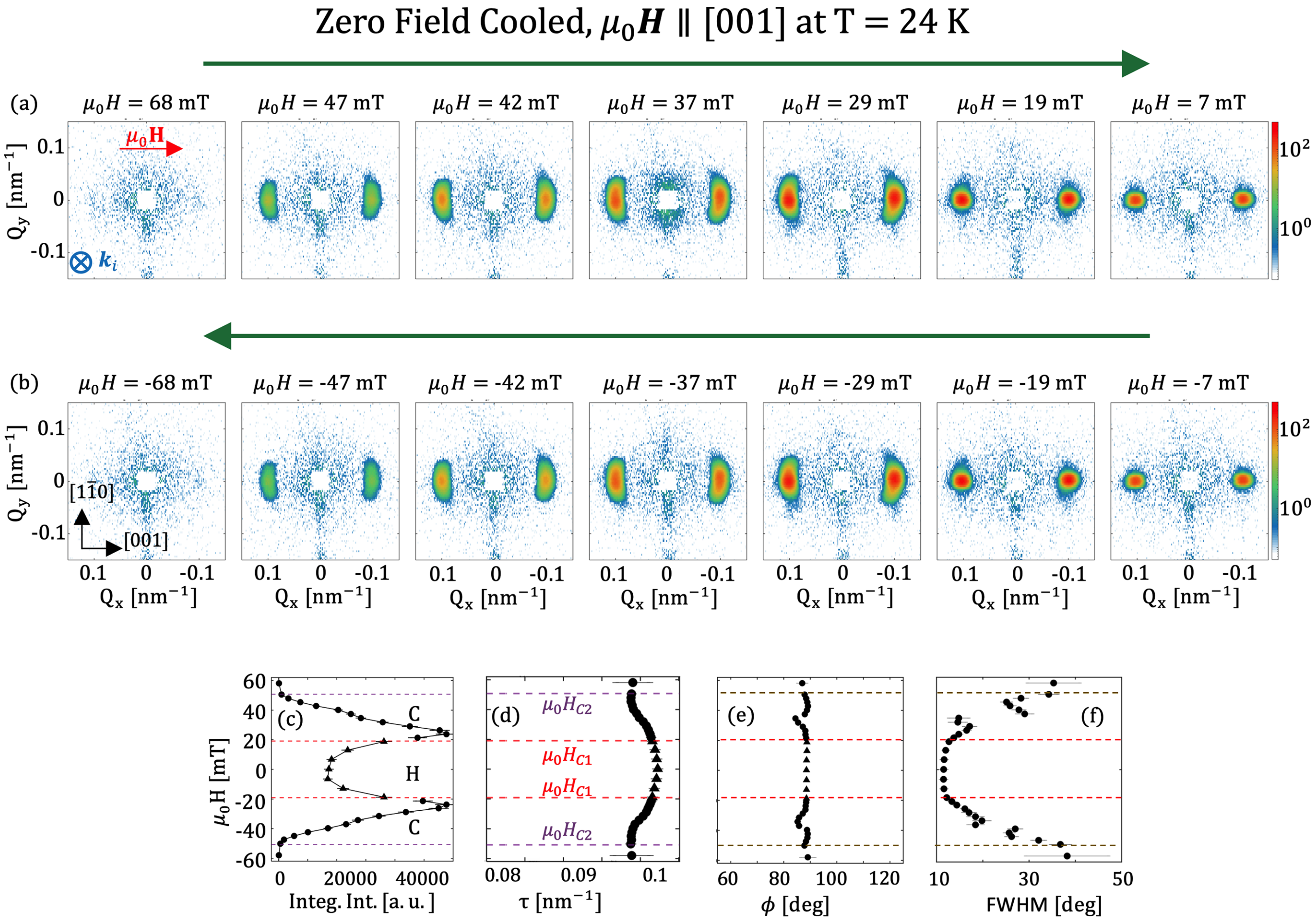

FIG. 11. (a) and (b) show SANS patterns recorded at $T = 24$ K for selected fields using the protocol schematically depicted in Figure 1 of the main text. The arrows above the SANS patterns indicate the direction of change of the magnetic field. The red arrow in the $\mu_0 H = 68$ mT panel indicates the direction of the applied magnetic field, while k_i the direction of the incoming neutron beam. The field dependency of the integrated intensity is shown in (c). The values of the characteristic wavenumbers τ are provided in (d). (e) shows the azimuthal position of the conical/helical and TS peaks and (f) their FHWM.

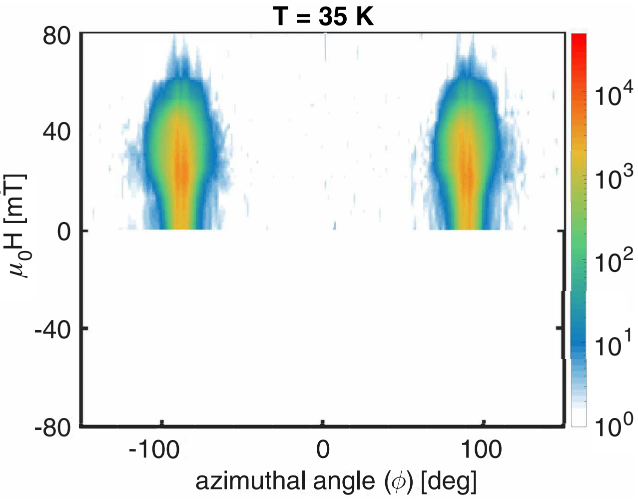

FIG. 12. Contour plot of the scattered intensity recorded between $Q = 0.05$ and $0.013\,\text{nm}^{-1}$ as a function of the azimuthal angle ϕ and the magnetic field for the $T = 35$ K. Here the measurements were performed only for positive fields.

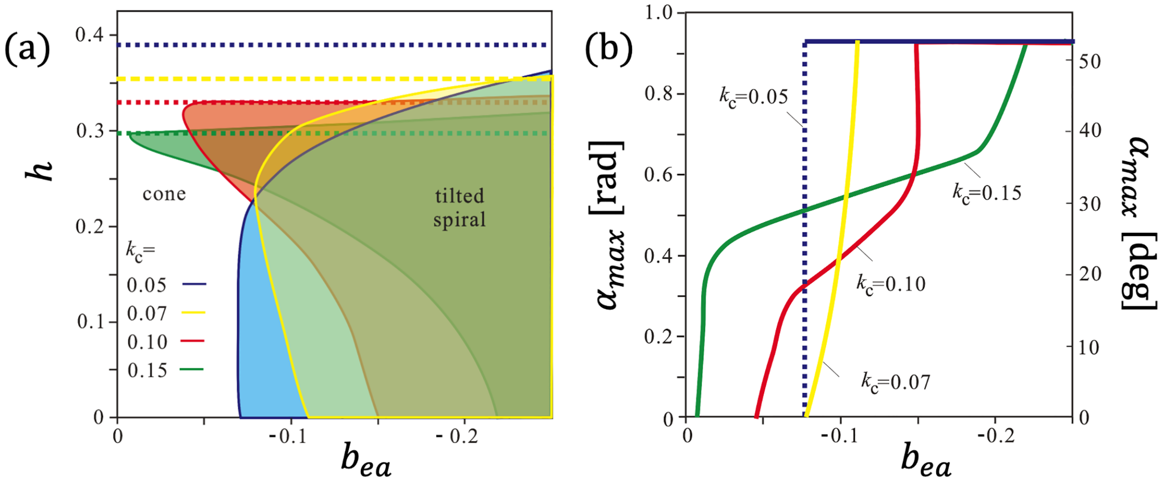

FIG. 13. Complementary results to Fig. 7 revealing the behaviour for $k_c = 0.07$: (a) phase diagram and (b) maximum tilt angle plotted as a function of b_{ea}.

[1] S. Muhlbauer, B. Binz, F. Jonietz, C. Pfleiderer, A. Rosch, A. Neubauer, R. Georgii, and P. Böni, Skyrmion lattice in a chiral magnet, Science **323**, 915 (2009).

[2] X. Z. Yu, Y. Onose, N. Kanazawa, J. H. Park, J. H. Han, Y. Matsui, N. Nagaosa, and Y. Tokura, Real-space observation of a two-dimensional skyrmion crystal, Nature (London) **465**, 901 (2010).

[3] H. Wilhelm, M. Baenitz, M. Schmidt, U. K. Rößler, A. A. Leonov, and A. N. Bogdanov, Precursor Phenomena at the Magnetic Ordering of the Cubic Helimagnet FeGe, Phys. Rev. Lett. **107**, 127203 (2011).

[4] S. Seki, X. Z. Yu, S. Ishiwata, and Y. Tokura, Observation of skyrmions in a multiferroic material, Science **336**, 198 (2012).

[5] P. Bak and M. H. Jensen, Theory of helical magnetic structures and phase transitions in MnSi and FeGe, J. Phys. C: Solid State Phys. **13**, L881 (1980).

[6] M. L. Plumer and M. B. Walker, Wavevector and spin reorientation in MnSi, J. Phys. C: Solid State Phys. **14**, 4689 (1981).

[7] A. Bauer, A. Chacon, M. Wagner, M. Halder, R. Georgii, A. Rosch, C. Pfleiderer, and M. Garst, Symmetry breaking, slow relaxation dynamics, and topological defects at the field-induced helix reorientation in MnSi, Phys. Rev. B **95**, 024429 (2017).

[8] S. V. Maleyev, Cubic magnets with Dzyaloshinskii-Moriya interaction at low temperature, Phys. Rev. B **73**, 174402 (2006).

[9] P. Milde, L. Köhler, E. Neuber, P. Ritzinger, M. Garst, A. Bauer, C. Pfleiderer, H. Berger, and L. M. Eng, Field-induced reorientation of helimagnetic order in Cu_2OSeO_3 probed by magnetic force microscopy, Phys. Rev. B **102**, 024426 (2020).

[10] S. Buhrandt and L. Fritz, Skyrmion lattice phase in three-dimensional chiral magnets from Monte Carlo simulations, Phys. Rev. B **88**, 195137 (2013).

[11] S. Seki, Y. Okamura, K. Shibata, R. Takagi, N. D. Khanh, F. Kagawa, T. Arima, and Y. Tokura, Stabilization of magnetic skyrmions by uniaxial tensile strain, Phys. Rev. B **96**, 220404(R) (2017).

[12] T. Nakajima, V. Ukleev, K. Ohishi, H. Oike, F. Kagawa, S. Seki, K. Kakurai, Y. Tokura, and T. Arima, Uniaxial-stress effects on helimagnetic orders and skyrmion lattice in Cu_2OSeO_3, J. Phys. Soc. Jpn. **87**, 094709 (2018).

[13] I. Levatić, P. Popčević, V. Šurija, A. Kruchkov, H. Berger, A. Magrez, J. S. White, H. M. Rønnow, and I. Živković, Dramatic pressure-driven enhancement of bulk skyrmion stability, Sci. Rep. **6**, 21347 (2016).

[14] M. Crisanti, N. Reynolds, I. Živković, A. Magrez, H. M. Rønnow, R. Cubitt, and J. S. White, In situ control of the helical and skyrmion phases in Cu_2OSeO_3 using high-pressure helium gas up to 5 kbar, Phys. Rev. B **101**, 214435 (2020).

[15] J. S. White, K. Prša, P. Huang, A. A. Omrani, I. Živković, M. Bartkowiak, H. Berger, A. Magrez, J. L. Gavilano, G. Nagy, J. Zang, and H. M. Rønnow, Electric-Field-Induced Skyrmion Distortion and Giant Lattice Rotation in the Magnetoelectric Insulator Cu_2OSeO_3, Phys. Rev. Lett. **113**, 107203 (2014).

[16] Y. Okamura, F. Kagawa, S. Seki, and Y. Tokura, Transition to and from the skyrmion lattice phase by electric fields in a magnetoelectric compound, Nat. Commun. **7**, 12669 (2016).

[17] A. J. Kruchkov, J. S. White, M. Bartkowiak, I. Živković, A. Magrez, and H. M. Rønnow, Direct electric field control of the skyrmion phase in a magnetoelectric insulator, Sci. Rep. **8**, 10466 (2018).

[18] J. S. White, I. Živković, A. J. Kruchkov, M. Bartkowiak, A. Magrez, and H. M. Rønnow, Electric-Field-Driven Topological Phase Switching and Skyrmion-Lattice Metastability in Magnetoelectric Cu_2OSeO_3, Phys. Rev. Appl. **10**, 014021 (2018).

[19] A. Štefančič, S. H. Moody, T. J. Hicken, M. T. Birch, G. Balakrishnan, S. A. Barnett, M. Crisanti, J. S. O. Evans, S. J. R. Holt, K. J. A. Franke, P. D. Hatton, B. M. Huddart, M. R. Lees, F. L. Pratt, C. C. Tang, M. N. Wilson, F. Xiao, and T. Lancaster, Origin of skyrmion lattice phase splitting in Zn-substituted Cu_2OSeO_3, Phys. Rev. Mater. **2**, 111402(R) (2018).

[20] A. S. Sukhanov, Praveen Vir, A. S. Cameron, H. C. Wu, N. Martin, S. Mühlbauer, A. Heinemann, H. D. Yang, C. Felser, and D. S. Inosov, Increasing skyrmion stability in Cu_2OSeO_3 by chemical substitution, Phys. Rev. B **100**, 184408 (2019).

[21] A. N. Bogdanov and D. A. Yablonskii, Thermodynamically stable 'vortices' in magnetically ordered crystals. The mixed state of magnets, Zh. Eksp. Teor. Fiz. **95**, 178 (1989) [Sov. Phys. JETP **68**, 101 (1989)].

[22] A. Bogdanov and A. Hubert, The stability of vortex-like structures in uniaxial ferromagnets, J. Magn. Magn. Mater. **195**, 182 (1999).

[23] U. K. Rößler, A. N. Bogdanov, and C. Pfleiderer, Spontaneous skyrmion ground states in magnetic metals, Nature (London) **442**, 797 (2006).

[24] A. O. Leonov, Twisted, localized, and modulated states described in the phenomenological theory of chiral and nanoscale ferromagnets, Ph.D. thesis, Technical University of Dresden, 2012.

[25] A. B. Butenko, A. A. Leonov, U. K. Rößler, and A. N. Bogdanov, Stabilization of skyrmion textures by uniaxial distortions in noncentrosymmetric cubic helimagnets, Phys. Rev. B **82**, 052403 (2010).

[26] F. Qian, L. J. Bannenberg, H. Wilhelm, G. Chaboussant, L. M. DeBeer-Schmitt, M. P. Schmidt, A. Aqeel, T. T. M. Palstra, E. H. Brück, A. J. E. Lefering, C. Pappas, M. Mostovoy, and A. O. Leonov, New magnetic phase of the chiral skyrmion material Cu_2OSeO_3, Sci. Adv. **4**, eaat7323 (2018).

[27] A. Chacon, L. Heinen, M. Halder, A. Bauer, W. Simeth, S. Mühlbauer, H. Berger, M. Garst, A. Rosch, and C. Pfleiderer, Observation of two independent skyrmion phases in a chiral magnetic material, Nat. Phys. **14**, 936 (2018).

[28] M. Halder, A. Chacon, A. Bauer, W. Simeth, S. Mühlbauer, H. Berger, L. Heinen, M. Garst, A. Rosch, and C. Pfleiderer, Thermodynamic evidence of a second skyrmion lattice phase and tilted conical phase in Cu_2OSeO_3, Phys. Rev. B **98**, 144429 (2018).

[29] L. J Bannenberg, H. Wilhelm, R. Cubitt, A. Labh, M. P Schmidt, E. Lelièvre-Berna, C. Pappas, M. Mostovoy, and A. O. Leonov, Multiple low-temperature skyrmionic states in a bulk chiral magnet, npj Quantum Mater. **4**, 11 (2019).

[30] O. Janson, I. Rousochatzakis, A. A. Tsirlin, M. Belesi, A. A. Leonov, U. K. Rößler, J. van den Brink, and H. Rosner, The quantum nature of skyrmions and half-skyrmions in Cu_2OSeO_3, Nat. Commun. **5**, 5376 (2014).

[31] I. E. Dzyaloshinskii, The theory of Helicoidal Structures in Antiferromagnets. II. Metals, Zh. Eksp. Teor. Fiz. **47**, 336 (1964) [Sov. Phys.–JETP **20**, 665 (1965)].

[32] A. O. Leonov and C. Pappas, Topological boundaries between helical domains as a nucleation source of skyrmions in the bulk cubic helimagnet Cu_2OSeO_3, Phys. Rev. Res. **4**, 043137 (2022).

[33] S. H. Moody, P. Nielsen, M. N. Wilson, D. A. Venero, A. Štefančič, G. Balakrishnan, and P. D. Hatton, Experimental evidence of a change of exchange anisotropy sign with temperature in Zn-substituted Cu_2OSeO_3, Phys. Rev. Res. **3**, 043149 (2021).

[34] I. Živković, D. Pajić, T. Ivek, and H. Berger, Two-step transition in a magnetoelectric ferrimagnet Cu_2OSeO_3, Phys. Rev. B **85**, 224402 (2012).

[35] See http://doi.org/10.5291/ILL-DATA.5-42-492.

[36] m.crisanti@tudelft.nl.

[37] c.pappas@tudelft.nl.

[38] leonov@hiroshima-u.ac.jp.

[39] A. O. Leonov, C. Pappas and I. I. Smalyukh, Field-driven metamorphoses of isolated skyrmions within the conical state of cubic helimagnets, Phys. Rev. B **104**, 064432 (2021).